Received 27 May 2020; accepted 15 June 2020. Date of publication 19 June 2020; date of current version 3 July 2020.

Digital Object Identifier 10.1109/OJCOMS.2020.3003742

Statistical Modeling of the Impact of Underwater Bubbles on an Optical Wireless Channel

MYOUNGKEUN SHIN, KI-HONG PARK (Senior Member, IEEE), AND MOHAMED-SLIM ALOUINI (Fellow, IEEE)

Computer, Electrical, and Mathematical Science and Engineering Division, King Abdullah University of Science and Technology, Thuwal 23955, Saudi Arabia

CORRESPONDING AUTHOR: K.-H. PARK (e-mail: kihong.park@kaust.edu.sa)

This work was supported by the King Abdullah University of Science and Technology.

ABSTRACT In underwater wireless optical communications (UWOC), the random obstruction of light propagation by air bubbles can cause fluctuations in the incoming light intensity of a receiver. In this paper, we propose a statistical model for determining the received power by a receiver in the presence of air bubbles. First, based on real experiments of the behavior of air bubbles underwater, we propose statistical models for the generation, size, and horizontal distribution of each air bubble. Second, we mathematically derive the obstruction caused by the shadow of each bubble as it passes over the beam area. We then compute the combined obstruction of all generated air bubbles to determine the total obstructed power, which is a random variable due to the randomness of bubble behavior. Next, we find the first and second moments of the total obstructed power to model the statistical distribution of the obstructed received power by using the method of moments, which shows that the Weibull distribution suitably matches the simulation data. We also estimate the shape and scale parameters by using two derived moments. Furthermore, we also construct a statistical model of the received power with complete blockage in the presence of air bubbles and we derive the distribution of the composite channel model combining the proposed bubble-obstruction model with a Gamma-Gamma turbulence model. Finally, we obtain and verify the analytic forms of the average bit error rate and the capacity of UWOC systems under this newly proposed composite channel model.

INDEX TERMS Underwater wireless optical communications, air bubbles, turbulence, and performance analysis.

I. INTRODUCTION

WIRELESS communications are a crucial component of several underwater applications such as tactical surveillance, pollution monitoring, oil control and maintenance, offshore oil explorations, climate change monitoring, and oceanography research [1]. Wireless underwater communications can be classified according to their means of communication, i.e., acoustic, radio frequency (RF), and optical.[1] Conventional acoustic communications can be transmitted over long distances, but the data transfer rate is limited to several kbps/Mbps. RF waves suffer from severe attenuation during propagation. In contrast, even though underwater wireless optical communication (UWOC) can travel over short distances up to 100m only, UWOC can transfer information at much higher data rates, in the order of a Gbps [2].

UWOC is restricted to short transmission distance because of environmental attenuation factors such as absorption and scattering. In this context, laser beam propagation can be characterized mathematically in the form of the radiative transfer equation (RTE) [3], [4], [5] and probabilistically by the Monte-Carlo simulation [6]. Extensive analytical, numerical and experimental research has been conducted [7]. However, although turbulence caused by random variations in temperature and salinity induces the fluctuations in beam power detected at the receiver, there has been relatively minimal research in this area. Most studies on underwater turbulence still apply the existing free-space optical (FSO) channel models such as lognormal distribution for the atmospheric environment, even though the atmospheric environment is quite different from the underwater environment.

1. Please see some table in more details which compares the pros and cons of acoustic and optical communications in [1].

The presence of air bubbles represents one of the main differences between the atmospheric and the underwater environment. For example, research oceanographer Grant B. Deane at the University of California, San Diego, calls our attention to bubbles in oceans. In large bodies of water, air bubbles are generated when waves break on the shore and sea surface [8]. The presence of bubbles may impact power fluctuations at the receiver. A recent study developed a statistical model of underwater turbulence induced by air bubbles based on real experiments [9], [10]. In those studies, the mixed exponential-Gamma distribution and exponential-lognormal distributions were proposed to model the statistics of received power, which is different from traditional lognormal distribution in the FSO turbulence model. Experimental results in [9] also showed that different bubble sizes and beam sizes affect power fluctuation at the receiver. Unfortunately, the probability that air bubbles perfectly block the optical propagation towards the receiver aperture was not considered in that proposed model, even though the experimental results showed that this situation can occur [10], [11].

To address this issue, here we newly develop a statistical model for the fluctuation of received power in UWOC systems under the randomness of air bubble generation, size and horizontal distribution. Based on these statistics of air bubbles, we calculate the expectation and the second moment of the obstructed received power. Using the method of moments, we propose a mixture of Weibull distribution and two Dirac delta functions in which the former represents partial blockage and the latter complete and no blockage. The main contributions of this work are as follows;

- Unlike the statistical model developed by experimental measurements in [9], [10], our proposed statistical model is purely mathematical and numerically solved by using the statistics of the generation, size, and the horizontal movement of a bubble.
- Our proposed statistical distribution more precisely models the effect of air bubbles on beam propagation by taking into consideration the probabilities of complete blockage and no blockage which are the most striking features differentiating from the aforementioned models in [9], [10].
- We provide the closed-form statistics of received signal-to-noise ratio (SNR) over composite channel model, which combines the proposed bubble-induced fading model and a Gamma-Gamma turbulence model.
- Finally, we analyze the ergodic capacity and the average bit error rate (BER).

The remainder of this paper is organized as follows. In Section II, we present the setup of the statistical model induced by air bubbles in underwater optical wireless channels. In Section III, we first delineate the overall strategy to find the fitted distribution and we then show the precision of predicted models compared with simulation data by using the mean-square-error (*MSE*) and the R^2 tests. In Section IV, we present the results of the performance analysis of the composite model and verify its accuracy by comparison with simulation results. Finally, some concluding remarks are given in Section V.

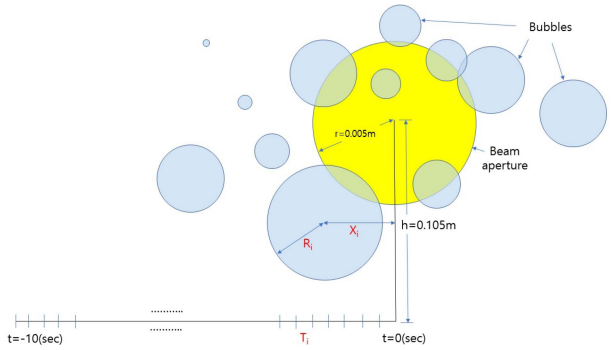

FIGURE 1. Example of air bubbles in a single layer rising around an optical beam on (w, z)-coordinate.

II. SYSTEM SETUP FOR THE STATISTICAL MODELING

The system setup for our statistical model is based on the models based on two real experiments discussed in previous works [9], [11]. We assume the system consists of a water tank with air bubbles emerging from the holes at the bottom of the tank. An optical beam is perfectly aligned to the receiver aperture and propagated from one wall of the tank to the opposite wall, where the receiver is located. Specifically, we assume that the optical beam has the following Gaussian distribution:

$$h(w, z) = \frac{1}{2\pi\sigma^2} \exp\left(-\frac{w^2 + z^2}{2\sigma^2}\right), \tag{1}$$

where $\sigma = 5$ [mm] is the variance related to the beam waist and (w, z)-coordinate spans the space perpendicular to the beam propagation. In [9], [11], the diameters of optical beam and active area at the photodiode at the receiver are nearly 4 [mm]. The optical beam diameter less than 10 [mm] in [11, Fig. 7] is shown to be reasonable to investigate the fluctuation of received power. Therefore, we assume that the beam aperture at the receiver is circular, and its radius is $r = 5$ [mm]. Here, we assume that transmit laser source and receiver aperture are embedded on the stand with a height of 10 [cm]. Accordingly, the beam center is assumed to be located at a height of 0.105 [m] from the bottom of the tank. We note that this specific value of beam center does not affect the simulation results since the time duration of generating air bubbles, which is 10 [sec], is long enough to span all the air bubbles affecting the received power regardless of a height of beam center. Fig. 1 illustrates the beam propagation in the presence of air bubbles around the receiver at (w, z)-coordinate. We outline the assumptions of the generation rate, the horizontal movement, and the sizes of bubbles in the following subsections in more detail.

A. RANDOM GENERATION OF AIR BUBBLES

We note that we calculate the received power at one time instant (current). Before that time instant, we assume that

each bubble is generated uniformly within its own specific time interval, which is related to the blow rate of air bubbles in the experiment. Every interval has the same length, only one bubble is generated in each interval, and the intervals do not overlap with each other. We also assume that the power is only obstructed by the bubbles that have been generated between the current time instant and 10 [sec] before that.[2] In this sense, the probability density function (PDF) of the time instant when generating the bubble in the ith time interval closest to the current time instant, T_i is given by

$$f_{T_i}(t) = \frac{1}{L}, \quad (i-1)L \le t \le iL, \tag{2}$$

where L is the length of an interval. We use four different lengths for simulation: 1/20, 1/40, 1/80, and 1/160 [sec], which provide different levels of obstruction of the beam propagation. The lower L is, the more bubbles are generated for the given 10 [sec] period.

B. HORIZONTAL MOVEMENT OF AIR BUBBLES

For simplicity, we assume only a single layer of bubbles originate from a single hole at the bottom of the tank, and the layer is parallel to the wall where the receiver is located. Although rising bubbles vibrate a bubble jitters a little when moving upwards, their horizontal movement cannot be considered as Brownian motion. It is also possible to assume multiple layers of bubbles by adding multiple independent bubbles in each interval, but in this paper, we only consider a single layer of bubbles. Thus, we assume that bubbles only move upwards and that the bubbles are distributed in a single layer according to a specific Gaussian distribution. Specifically, as shown in Fig. 1, the minimum distance of a bubble from the line that goes through the center of the beam and is perpendicular to the bottom of the tank is assumed to be a Gaussian random variable X_i with zero mean and variance σ_x^2. We assume that the standard deviation $\sigma_x = \sigma$ is the same as the radius of the beam aperture, which is 5 [mm]. As the standard deviation of X_i, 5 [mm] is less than the actual deviations in the real experiments shown in [11, Fig. 5]. We note that this can emphasize the effect of the obstruction due to the multiple air bubbles on light propagation. The distribution of horizontal distance X_i is given by

$$f_{X_i}(x) = \frac{1}{\sqrt{2\pi\sigma^2}} e^{-\frac{x^2}{2\sigma^2}}. \tag{3}$$

C. VERTICAL MOVEMENT OF AIR BUBBLES

Here, we describe the vertical movement of air bubbles to quantify the vertical distance of a bubble from the center of the optical beam, which is closely related to the generation time (explained in Section II-B) and the rising velocity of an air bubble, which depends on the size-dependent bubble shape. Moreover, using the upper limit on the area of a bubble shown in [11, Fig. 5], we assume there the bubble size does not exceed 0.01 [m]. Accordingly, the distribution of R_i is represented by

$$f_{R_i}(r;\mu_{R_i}) = \frac{\pi r}{2{\mu_{R_i}}^2} e^{\frac{-\pi r^2}{4{\mu_{R_i}}^2}} \Big/ q, \quad 0 \le r \le 0.01, \tag{4}$$

where $q = \int_0^{0.01} \frac{\pi r}{2{\mu_{R_i}}^2} e^{\frac{-\pi r^2}{4{\mu_{R_i}}^2}} dr$ is the normalization factor and μ_{R_i} is the mean of the radius of bubbles. Here, we consider four different values of μ_{R_i} for simulation, i.e., 1.36 [mm], 1.50 [mm], 1.95 [mm], and 2.99 [mm], respectively. We note that these four specific values are derived from the mean area of air bubbles in [11, Fig. 5].

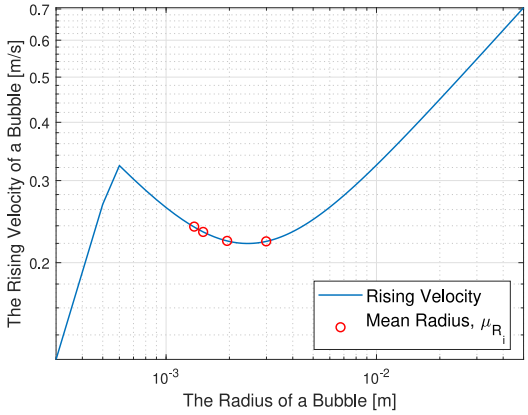

FIGURE 2. Rising velocity of a bubble in water [12].

The rising velocity of an air bubble changes mainly because of its diameter and shape. More specifically, the bubble has three types of shape; sphere, spheroid, and spherical cap [12]. Fig. 2 shows how the rising velocity of a bubble changes as its diameter increases. When a bubble is very small, it is spherical because the inertial force is small compared to the viscous force, and its rising velocity increases as it grows in size because of the dominance of buoyancy. As its size further increases, the inertial force becomes tangible and the increasing rate of the rising velocity begins to slow down. When it becomes even bigger in size, the bubble changes its shape from sphere to spheroid, and its rising velocity starts to decrease because the friction becomes tangible. However, the rising velocity increases again as the ratio of the longer axis length to the shorter axis length increases. When the bubble becomes much bigger, the bubble changes its shape from spheroid to spherical cap. The rising velocity of the bubble, v [m/s], is given by [12]

$$v = \begin{cases} \frac{g\rho {R_i}^2}{3\mu}, & 0 < R_i < 0.08015 \text{ [mm]} \\ 0.408 g^{\frac{5}{6}} \left(\frac{\rho}{\mu}\right)^{\frac{2}{3}} {R_i}^{\frac{3}{2}}, & 0.08015 \le R_i < 0.575 \text{ [mm]} \\ \sqrt{\frac{1.07\rho}{\sigma_s R_i} + 1.01 g R_i}, & R_i \ge 0.575 \text{ [mm]}, \end{cases} \tag{5}$$

where R_i [m] is the radius of a bubble, ρ is the density of the liquid medium, σ_s is the surface tension of the liquid

2. The reason why we only consider 10 [sec] is that the bubbles generated before 10 [sec] do not cause any significant obstruction. More specifically, relatively big bubbles travel up the aperture faster due to their faster rising velocity, while the influence on the obstruction by relatively small bubbles is minimal.

medium, and g is gravitational acceleration. In order to calculate the area in aperture obstructed by air bubbles at the specific vertical position of current time instance, we can determine the vertical position of air bubble by multiplying the rising time duration with the rising velocity related to the generated bubble's radius. Here we remark that, even though we admit that it is more realistic to use all possible bubble shapes, it is highly difficult to calculate the overlapped areas with spheroid/spherical cap-shaped bubbles. Therefore, we assume that all bubbles are spherical when it comes to the calculation, while we use (5) as the rising velocity.

III. PROPOSED STATISTICAL MODEL FOR BUBBLE OBSTRUCTION

It is very difficult to find the explicit PDF of the obstructed power due to the air bubbles directly from the statistical models of bubble behavior. Therefore, we will use the method of moments, which compares the moments of the derived statistical model and a well-known distribution, and estimates the parameters of the distribution so that their moments match each other [13]. We will go through the following procedures.

1) Let the random variables B_i be the amount of obstructed power due to the ith bubble and B_i can be expressed as a function of X_i, R_i, and T_i.

$$\begin{aligned} B_i &= b_i(X_i, R_i, T_i) \\ &= B_i^{(1)} \mathbb{1}_{(0,|r-R_i|)}(D_i)\mathbb{1}_{(0,r)}(R_i) \\ &\quad + B_i^{(2)} \mathbb{1}_{\left(|r-R_i|,\sqrt{r^2-R_i^2}\right)}(D_i)\mathbb{1}_{(0,r)}(R_i) \\ &\quad + B_i^{(3)} \mathbb{1}_{\left(\sqrt{r^2-R_i^2},(r+R_i)\right)}(D_i)\mathbb{1}_{(0,r)}(R_i) \\ &\quad + B_i^{(4)} \mathbb{1}_{(0,|r-R_i|)}(D_i)\mathbb{1}_{(0,R_i)}(r) \\ &\quad + B_i^{(5)} \mathbb{1}_{\left(|r-R_i|,\sqrt{R_i^2-r^2}\right)}(D_i)\mathbb{1}_{(0,R_i)}(r) \\ &\quad + B_i^{(6)} \mathbb{1}_{\left(\sqrt{R_i^2-r^2},(r+R_i)\right)}(D_i)\mathbb{1}_{(0,R_i)}(r), \end{aligned} \tag{6}$$

where $B_i^{(j)}$ $(j = 1, 2, \ldots, 6)$ indicates the obstructed power for the various cases of a bubble's location with respect to the beam and D_i denotes the distance between the centers of a bubble and the aperture. The details of deriving each $B_i^{(j)}$ are delineated in Appendix B. Also, $\mathbb{1}_{\mathcal{S}}(x)$ is an indicator function that is defined as

$$\mathbb{1}_{\mathcal{S}}(x) = \begin{cases} 1, & x \in \mathcal{S} \\ 0, & x \notin \mathcal{S}. \end{cases} \tag{7}$$

2) Defining the sum of B_i, $\forall i$, as a random variable B, we calculate the expectation and the second moment of B. The formulas are described in detail in Appendix C.
3) We can model the PDF of B as given by

$$f_B(x) = a\delta(x) + bf_W(x), \ x \geq 0, \tag{8}$$

where $\delta(x)$ is the Dirac delta function, a is the probability of no power obstruction, and $b = 1 - a$ is the probability of any power obstruction. $f_W(x)$ is the normalized density distribution of power obstruction for $x > 0$, which is modeled as the Weibull distribution given by

$$f_W(x) = \frac{k}{\lambda}\left(\frac{x}{\lambda}\right)^{k-1} e^{(x/\lambda)^k}, \quad x \geq 0, \tag{9}$$

where λ and k are the scale and shape parameters. With the first and second moments of B, we estimate the scale and shape parameters of the Weibull distribution. The details are described in Appendix D.
4) The power obstructed by air bubbles cannot exceed the maximum received power onto the beam aperture, i.e., $m = \int_{\mathcal{A}} h(w, z)\, dw\, dz$, where $\mathcal{A}$ is the beam aperture area without any obstruction. Then, we modify the PDF of B to the following form

$$f_B(x) = a\delta(x) + bf_W(x) + c\delta(x - m), \ 0 \leq x \leq m, \tag{10}$$

where $c = \int_m^{\infty} bf_W(x)dx$ indicates the complete obstruction of the received power.
5) Finally, we can obtain the distribution of the received power in the presence of air bubble obstruction at the receiver as

$$f_{H_b}(x) = c\delta(x) + bf_W(m - x) + a\delta(x - m), \ 0 \leq x \leq m. \tag{11}$$

A. THE RESULTS OF THE PARAMETER ESTIMATION IN $F_{H_B}(X)$

In Table 1, we provide the values of parameters a, b and c when we use the Gaussian beam that we described in the previous sections. We also provide the comparison of the estimated distribution $f_{h_b}(x)$ and the simulation data. For the simulation data, a means the probability of no power obstruction and c means the complete obstruction.

In all four cases of the bubble generation rate, as the average radius of the bubbles increases, the chance of power obstruction increases. Furthermore, as the generation rate increases with the average increase in the radius, there is increased chance of power obstruction. When the average of the radius is 1.35 [mm], and the rate is 20 [1/sec], the probability of no power obstruction is above 0.42. On the other hand, when the average of the radius is 2.99 [mm], and the rate is 160 [1/sec], the probability of complete power failure is 0.76. We can check that the values of the parameters a, b, and c are very close to simulation data. From the comparison between our proposed statistical model and simulation data, we can see the relation between the system parameters considered in our model and the estimated parameters for blockage on the beam propagation as in Table 2 below.

B. THE RESULTS OF FIT TESTS

In this section, we present the goodness of fit for two tests, which are the *MSE* test and the R^2 test. The definition of the *MSE* test is given by

$$MSE = \frac{\sum_{i=1}^{N}[F_s(I_i) - F(I_i)]^2}{N}, \tag{12}$$

TABLE 1. The parameters and test results for bubble generation rates of 20, 40, 80 and 160 [1/sec].

Distribution		Simulation Data			Proposed Distribution						
Rate [1/sec]	Radius [mm]	Parameters			Parameters					Test Results	
		c	b	a	c	b	a	k	λ	MSE	R^2
20	1.35	0	0.58	0.42	3.28E-6	0.58	0.42	0.935	0.030	3.43E-5	0.997
	1.50	5.00E-5	0.60	0.40	1.41E-5	0.60	0.40	0.955	0.036	3.27E-5	0.998
	1.95	6.30E-4	0.67	0.33	4.92E-4	0.66	0.34	0.968	0.054	2.50E-5	0.998
	2.99	0.02	0.74	0.26	0.01	0.75	0.25	0.983	0.102	1.30E-4	0.996
40	1.35	0	0.82	0.18	2.36E-5	0.82	0.18	1.307	0.044	6.97E-5	0.985
	1.50	1.40E-4	0.84	0.16	1.04E-4	0.84	0.16	1.064	0.053	6.61E-5	0.987
	1.95	3.40E-3	0.89	0.11	2.80E-3	0.89	0.11	1.110	0.085	3.88E-5	0.990
	2.99	0.07	0.94	0.06	0.06	0.94	0.06	1.170	0.172	1.92E-4	0.986
80	1.35	3.90E-4	0.97	0.03	2.16E-4	0.97	0.03	1.290	0.079	5.98E-5	0.944
	1.50	1.50E-3	0.97	0.03	1.00E-3	0.98	0.02	1.400	0.097	5.18E-5	0.941
	1.95	0.03	0.99	0.01	0.03	0.99	0.01	1.448	0.162	1.79E-5	0.976
	2.99	0.29	1	3.80E-3	0.28	1	3.30E-3	1.590	0.343	1.67E-5	1.000
160	1.35	0.01	1	7.50E-4	4.70E-3	1	9.25E-4	1.806	0.160	6.38E-6	0.971
	1.50	0.03	1	5.70E-4	0.02	1	5.96E-4	1.892	0.197	1.18E-5	0.978
	1.95	0.22	1	1.50E-4	0.22	1	1.27E-4	2.087	0.328	9.0E-5	0.998
	2.99	0.77	1	0	0.76	1	1.03E-5	0.231	0.692	4.41E-5	1.000

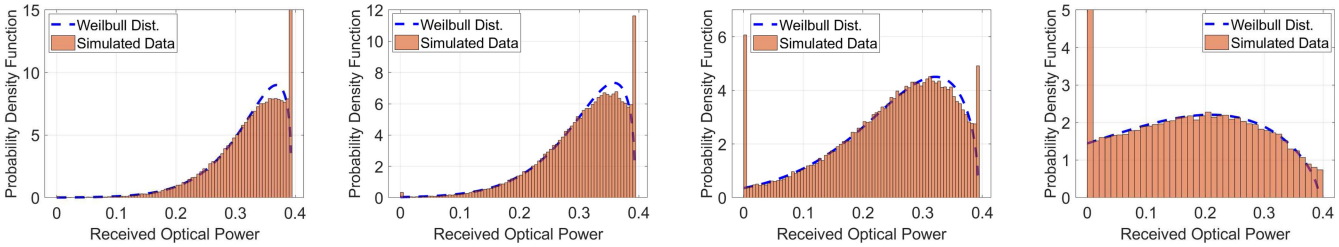

(a) Radius(μ_R): 1.35 [mm] (b) Radius(μ_R): 1.50 [mm] (c) Raduis(μ_R): 1.95 [mm] (d) Radius(μ_R): 2.99 [mm]

FIGURE 3. The distributions of the four different radii of bubbles when the bubble generation rate is 80 [1/sec]. The areas of first and last peak bars in histogram of simulated data indicate the probabilities of complete blockage (*c*) and no blockage (*a*) which is not drawn for our proposed statistical model.

TABLE 2. The tendency of estimated parameters with respect to the system parameters.

System Parameters	Estimated Parameters	
	Perfect blockage c	No blockage a
Radius of Aperture r ($\nearrow$)	$\searrow$	$\searrow$
Radius of Air Bubble μ_{R_i} ($\nearrow$)	$\nearrow$	$\searrow$
Horizontal Movement σ_x ($\nearrow$)	$\searrow$	$\nearrow$
Bubble Arrival L ($\nearrow$)	$\searrow$	$\nearrow$

where $F_s(I_i)$ is the value of the accumulated probability function of the simulation data at certain points I_i and $F(I_i)$ is the value of the cumulative distribution function (CDF) of the distribution, $f_{h_b}(x)$, at certain points I_i. When it comes to the goodness of fit of the *MSE* test, the closer the value is to 0, the better the fit is.

The R^2 test metric is defined as

$$R^2 = 1 - \frac{S_e}{S_t}, \tag{13}$$

where $S_e = \sum_{i=1}^{M}(f_{s,i} - f_{p_i})^2$ and $S_t = \sum_{i=1}^{M}(f_{s,i} - \bar{f})^2$, $f_{s,i}$ and $f_{p,i}$ are the probability of the simulated data and $f_{h_b}(x)$ at the ith interval, $\bar{f}$ is the mean of $f_{s,i}$ and M is the number of the intervals. When it comes to the goodness of fit of the R^2 test, the closer the value is to 1, the better the fit is.

Table 1 shows the results of goodness of fit tests for our proposed model. For all cases, the *MSE* test results are close to 0 and the R^2 test results are close to 1. We note that the distribution of the received power is the lower bound of actual received power because we calculate the sum of obstructed powers between every bubble and the beam area but we neglect the fact that the bubbles cannot overlap. The discrepancy between actual distribution and the proposed model increases as the generation rate and average size of air bubbles increase.

C. COMPARISON BETWEEN SIMULATION AND STATISTICAL MODEL

Fig. 3 shows how the simulation data and its corresponding distribution are drawn, specifically for the cases of four different bubble radii with a bubble generation speed of 80 [1/sec]. We note in Fig. 3 that the areas of first and last peak bars in histogram of simulated data converge to the probabilities of complete blockage (c) and no blockage (a) as the bin size decreases. For our proposed statistical

model, we only draw the continuous part regarding Weibull distribution.

We can see that the simulation data matches its predicted distribution. The left tail of each distribution in particular matches very well, which is very important to predict average BER. Moreover, we note that the cases with no obstruction and full obstruction were considered, which were ignored in the previous work of [9].

IV. PERFORMANCE ANALYSIS

Underwater turbulence due to salinity and temperature variations can commonly cause a fluctuation in the received power. To evaluate the performance in UWOC channels in the presence of air bubbles and underwater turbulence, we combine the distribution of our proposed bubble obstruction model with another independent turbulence distribution. We first derive the composite PDF of received signal-to-noise ratio (SNR) over air bubble obstruction and Gamma-Gamma turbulence and analyze the ergodic capacity and average BER. The received signal can be written as

$$y = hx + n, \tag{14}$$

where x is the transmitted intensity, h is the channel state, and n is additive white Gaussian noise (AWGN) with zero mean and variance σ_n^2. The channel state h consists of three factors, i.e., $h = h_l h_a h_b$ with path loss h_l, turbulence h_a, and bubble obstruction h_b. These factors are independent of each other, and h_l is deterministic, whereas h_a and h_b follow the aforementioned statistical distributions. Here we assume that the beam is a Gaussian beam perfectly aligned to the receiver aperture and the turbulence fading distribution is Gamma-Gamma fading channel for strong turbulence underwater environments. We now derive the statistics of received SNR over composite channel models by combining our proposed bubble obstruction model with the Gamma-Gamma fading model.

A. STATISTICS OF RECEIVED SNR

We can write the instantaneous received SNR as follows:

$$\gamma = \frac{|h|^2 \mathbb{E}[x^2]}{\mathbb{E}[n^2]} = |h|^2 \bar{\gamma}, \tag{15}$$

where $\bar{\gamma} = \frac{\mathbb{E}[x^2]}{\mathbb{E}[n^2]}$ is defined as average SNR. Since $\bar{\gamma}$ and h_l are constant, we first find the CDF of $h_{ab} = h_a h_b$, which is computed as

$$\begin{aligned} F_{H_{ab}}(x) &= \Pr(H_a H_b \le x) \\ &= \int_0^\infty F_{H_a}\left(\frac{x}{y}\right) f_{H_b}(y) dy \\ &= \int_0^\infty F_{H_a}\left(\frac{x}{y}\right) (c\delta(y) + b f_W(1-y) + a\delta(y-1)) dy \\ &= c + b\int_0^1 F_{H_a}\left(\frac{x}{y}\right) f_W(1-y)\, dy + a F_{H_a}(x), \end{aligned} \tag{16}$$

where we note that $m = 1$ due to the average SNR $\bar{\gamma}$, and $F_{H_a}(\cdot)$ is the CDF of a Gamma-Gamma distribution whose PDF is given by $f_{H_a}(x) = \frac{2(\alpha\beta)^{(\alpha+\beta)/2}}{\Gamma(\alpha)\Gamma(\beta)} x^{\frac{\alpha+\beta}{2}-1} K_{\alpha-\beta}(2\sqrt{\alpha\beta x})$ where $K_\alpha(x)$ is the modified Bessel function of the second kind [14].

Due to the analytical intractability of integration, we use the Gauss-Legendre quadrature method to approximate the second term as follows:

$$\begin{aligned} &\int_0^1 F_{H_a}\left(\frac{x}{y}\right) f_W(1-y) dy \\ &\quad \approx \frac{1}{2}\sum_{i=1}^n w_i F_{H_a}\left(\frac{2x}{x_i+1}\right) f_W\left(\frac{1-x_i}{2}\right), \end{aligned} \tag{17}$$

where w_i and x_i are the weight and the abscissa, and $w_i = \frac{2}{(1-x_i^2)[P_n'(x_i)]^2}$ with Legendre polynomials $P_n(x)$. Therefore,

$$F_{H_{ab}}(x) \approx c + \frac{b}{2}\sum_{i=1}^n w_i F_{H_a}\left(\frac{2x}{x_i+1}\right) f_W\left(\frac{1-x_i}{2}\right) + a F_{H_a}(x). \tag{18}$$

Accordingly, the channel gain $h = h_l h_a l_b$ and the received SNR γ can be computed by change of variables as

$$\begin{aligned} F_H(x) \approx c &+ \frac{b}{2}\sum_{i=1}^n w_i F_{H_a}\left(\frac{2x}{h_l(x_i+1)}\right) f_W\left(\frac{1-x_i}{2}\right) \\ &+ a F_{H_a}\left(\frac{x}{h_l}\right) \end{aligned} \tag{19}$$

and

$$\begin{aligned} F_\gamma(x) \approx c &+ \frac{b}{2}\sum_{i=1}^n w_i F_{H_a}\left(\frac{2\sqrt{x}}{h_l\sqrt{\bar{\gamma}}(x_i+1)}\right) f_W\left(\frac{1-x_i}{2}\right) \\ &+ a F_{H_a}\left(\frac{\sqrt{x}}{h_l\sqrt{\bar{\gamma}}}\right), \end{aligned} \tag{20}$$

respectively. Therefore, the PDF of γ is given by

$$\begin{aligned} f_\gamma(x) \approx c\delta(x) &+ \frac{b}{2}\sum_{i=1}^n C_i^{(0)} x^{-1/2} f_{H_a}\left(\frac{2\sqrt{x}}{h_l\sqrt{\bar{\gamma}}(x_i+1)}\right) \\ &+ a C_0^{(0)} x^{-1/2} f_{H_a}\left(\frac{\sqrt{x}}{h_l\sqrt{\bar{\gamma}}}\right), \end{aligned} \tag{21}$$

where $C_i^{(0)} = \frac{w_i}{h_l\sqrt{\bar{\gamma}}(x_i+1)} f_W(\frac{1-x_i}{2})$ and $C_0^{(0)} = \frac{1}{2h_l\sqrt{\bar{\gamma}}}$.

B. ERGODIC CAPACITY

The ergodic channel capacity $\bar{C}$ is defined as $\bar{C} = \mathbb{E}[\log_2(1+\gamma)]$. We represent $\log(1+\gamma)$ as $G_{2,2}^{1,2}\left(\begin{smallmatrix}1,1\\1,0\end{smallmatrix}\middle|\,\gamma\right)$ and the modified Bessel function of the second kind $K_v(x)$ as $\frac{1}{2}G_{0,2}^{2,0}\left(\begin{smallmatrix}-\\ \frac{v}{2},-\frac{v}{2}\end{smallmatrix}\middle|\,\frac{x^2}{4}\right)$ using Meijer's G function [15].

$$\begin{aligned} \mathbb{E}\big[\log_2(1+\gamma)\big] &= \int_0^\infty \log_2(1+\gamma) f_\gamma(\gamma)\, d\gamma \\ &\approx \sum_{i=1}^n C_i^{(1)} \int_0^\infty \gamma^{\frac{\alpha+\beta}{4}-1} G_{2,2}^{1,2}\left(\begin{smallmatrix}1,1\\1,0\end{smallmatrix}\middle|\,\gamma\right) \\ &\quad \times G_{0,2}^{2,0}\left(\begin{smallmatrix}-\\ \frac{\alpha-\beta}{2},-\frac{\alpha-\beta}{2}\end{smallmatrix}\middle|\,\frac{2\alpha\beta}{h_l\sqrt{\bar{\gamma}}(x_i+1)}\gamma^{1/2}\right) d\gamma \end{aligned}$$

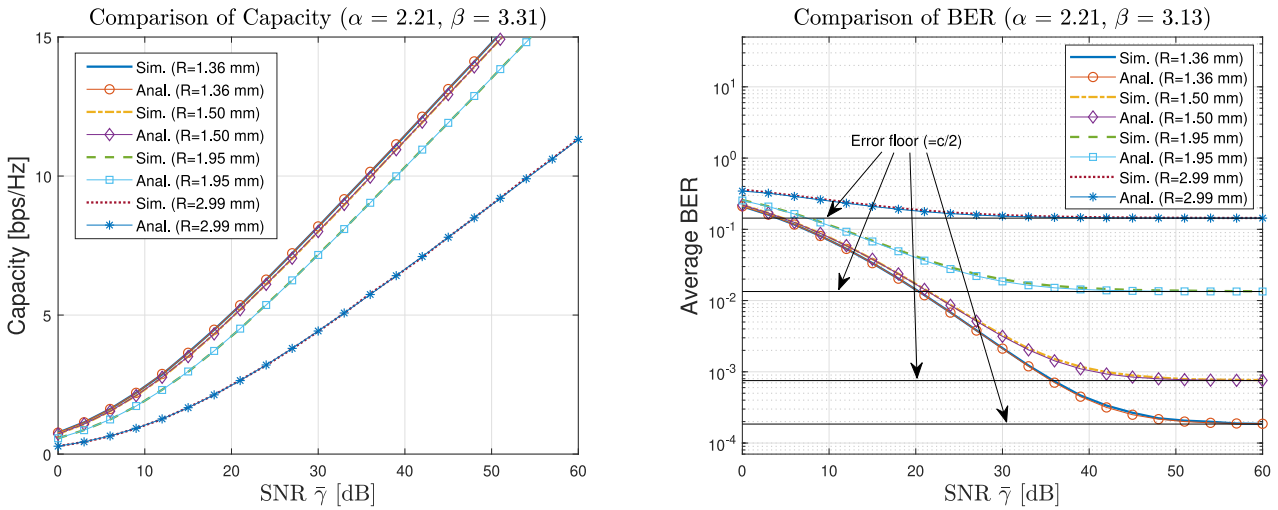

(a) Ergodic Capacity (b) Average BER

FIGURE 4. The results of the performance analysis with respect to different horizontal movement under the given generation rate of 80 [1/sec] and horizontal movement of $\sigma_X = 5$ [mm] of a bubble.

$$+ C_0^{(1)} \int_0^\infty \gamma^{\left(\frac{\alpha+\beta}{4}-1\right)} G_{2,2}^{1,2}\left(\begin{matrix}1,1\\1,0\end{matrix}\middle|\,\gamma\right) \times G_{0,2}^{2,0}\left(\begin{matrix}-\\ \frac{\alpha-\beta}{2},-\frac{\alpha-\beta}{2}\end{matrix}\middle|\,\frac{\alpha\beta}{h_l\sqrt{\bar{\gamma}}}\gamma^{1/2}\right) d\gamma, \quad (22)$$

where $C_i^{(1)} = \frac{bC_i^{(0)}}{2\log 2}\frac{(\alpha\beta)^{(\alpha+\beta)/2}}{\Gamma(\alpha)\Gamma(\beta)}\left(\frac{2}{h_l\sqrt{\bar{\gamma}}(x_i+1)}\right)^{\frac{\alpha+\beta}{2}-1}$ and $C_0^{(1)} = \frac{aC_0^{(0)}}{\log 2}\frac{(\alpha\beta)^{(\alpha+\beta)/2}}{\Gamma(\alpha)\Gamma(\beta)}\left(\frac{1}{h_l\sqrt{\bar{\gamma}}}\right)^{\frac{\alpha+\beta}{2}-1}$. Using [16, eq. (21)], we can express the ergodic capacity with Meijer's G function, which is given on the top of next page by (23), as shown at the bottom of the page, where $z_i = \frac{2\alpha\beta}{h_l\sqrt{\bar{\gamma}}(x_i+1)}$ and $z_0 = \frac{\alpha\beta}{h_l\sqrt{\bar{\gamma}}}$.

C. AVERAGE BER

The average BER is defined as $P_b = \mathbb{E}[Q(p\sqrt{q\gamma})]$, where $Q(\cdot)$ is the Q-function and p and q are modulation-depending parameters. Here, we use $p = 1$ and $q = 2$ for simulation. We note that $Q(x) = \frac{1}{2}\,\mathrm{erfc}(\frac{x}{\sqrt{2}})$ and $\mathrm{erfc}(\sqrt{x})$ can be expressed as $\mathrm{erfc}(\sqrt{x}) = \frac{1}{\sqrt{\pi}} G_{1,2}^{2,0}\left(\begin{matrix}1\\0,\frac{1}{2}\end{matrix}\middle|\,x\right)$ in the form of Meijer's G function [17]. Then, we can derive the average BER as

$$\begin{aligned} P_b &= \int_0^\infty Q\big(p\sqrt{q\gamma}\big) f_\gamma(\gamma)\, d\gamma \\ &= \frac{1}{2}\int_0^\infty \mathrm{erfc}\left(p\sqrt{\frac{q\gamma}{2}}\right) f_\gamma(\gamma)\, d\gamma \\ &\approx \frac{c}{2} + \sum_{i=1}^{n} C_i^{(2)} \int_0^\infty \gamma^{\frac{\alpha+\beta}{4}-1} G_{1,2}^{2,0}\left(\begin{matrix}1\\0,\frac{1}{2}\end{matrix}\middle|\,\frac{p^2 q}{2}\gamma\right) \\ &\quad \times G_{0,2}^{2,0}\left(\begin{matrix}-\\ \frac{\alpha-\beta}{2},-\frac{\alpha-\beta}{2}\end{matrix}\middle|\,\frac{2\alpha\beta}{h_l\sqrt{\bar{\gamma}}(x_i+1)}\gamma^{1/2}\right) d\gamma \\ &\quad + C_0^{(2)} \int_0^\infty \gamma^{\frac{\alpha+\beta}{4}-1} G_{1,2}^{2,0}\left(\begin{matrix}1\\0,\frac{1}{2}\end{matrix}\middle|\,\frac{p^2 q}{2}\gamma\right) \\ &\quad \times G_{0,2}^{2,0}\left(\begin{matrix}-\\ \frac{\alpha-\beta}{2},-\frac{\alpha-\beta}{2}\end{matrix}\middle|\,\frac{\alpha\beta}{h_l\sqrt{\bar{\gamma}}}\gamma^{1/2}\right) d\gamma, \end{aligned} \quad (24)$$

where $C_i^{(2)} = \frac{bC_i^{(0)}}{2\sqrt{\pi}}\frac{(\alpha\beta)^{(\alpha+\beta)/2}}{\Gamma(\alpha)\Gamma(\beta)}\left(\frac{2}{h_l\sqrt{\bar{\gamma}}(x_i+1)}\right)^{\frac{\alpha+\beta}{2}-1}$ and $C_0^{(2)} = \frac{aC_0^{(0)}}{\sqrt{\pi}}\frac{(\alpha\beta)^{(\alpha+\beta)/2}}{\Gamma(\alpha)\Gamma(\beta)}\left(\frac{1}{h_l\sqrt{\bar{\gamma}}}\right)^{\frac{\alpha+\beta}{2}-1}$. Using [16, eq. (21)], we can express the average BER with Meijer's G function on the bottom of the next page in (25).

D. NUMERICAL RESULTS

In this subsection, we validate our analytic results with comparison to the simulation results. For simulation set-up, we assume that the path loss for signal attenuation is assumed to be normal, i.e., $h_l = 1$ without loss of generality and we use $\alpha = 2.21$, $\beta = 3.31$ for the two parameters of the Gamma-Gamma distribution from [18].[3] The simulated results are evaluated with random samples of composite channel gains generated by multiplying our simulation data for air bubble obstruction with Gamma-Gamma distributed random realizations. We compare the performance results obtained by

3. We note that another set of parameters (α, β) for different underwater turbulence related to the salinity and temperature variation can be found by using the methods in [19], [20].

$$\bar{C} \approx \sum_{i=1}^{n} \frac{C_i^{(1)}}{2\pi} G_{2,6}^{6,1}\left(\begin{matrix}-\frac{\alpha+\beta}{4},1-\frac{\alpha+\beta}{4}\\ \frac{\alpha-\beta}{4},\frac{\alpha-\beta+2}{4},-\frac{\alpha-\beta}{4},-\frac{\alpha-\beta-2}{4},-\frac{\alpha+\beta}{4},-\frac{\alpha+\beta}{4}\end{matrix}\middle|\,\frac{{z_i}^2}{16}\right) + \frac{C_0^{(1)}}{2\pi} G_{2,6}^{6,1}\left(\begin{matrix}-\frac{\alpha+\beta}{4},1-\frac{\alpha+\beta}{4}\\ \frac{\alpha-\beta}{4},\frac{\alpha-\beta+2}{4},-\frac{\alpha-\beta}{4},-\frac{\alpha-\beta-2}{4},-\frac{\alpha+\beta}{4},-\frac{\alpha+\beta}{4}\end{matrix}\middle|\,\frac{{z_0}^2}{16}\right) \quad (23)$$

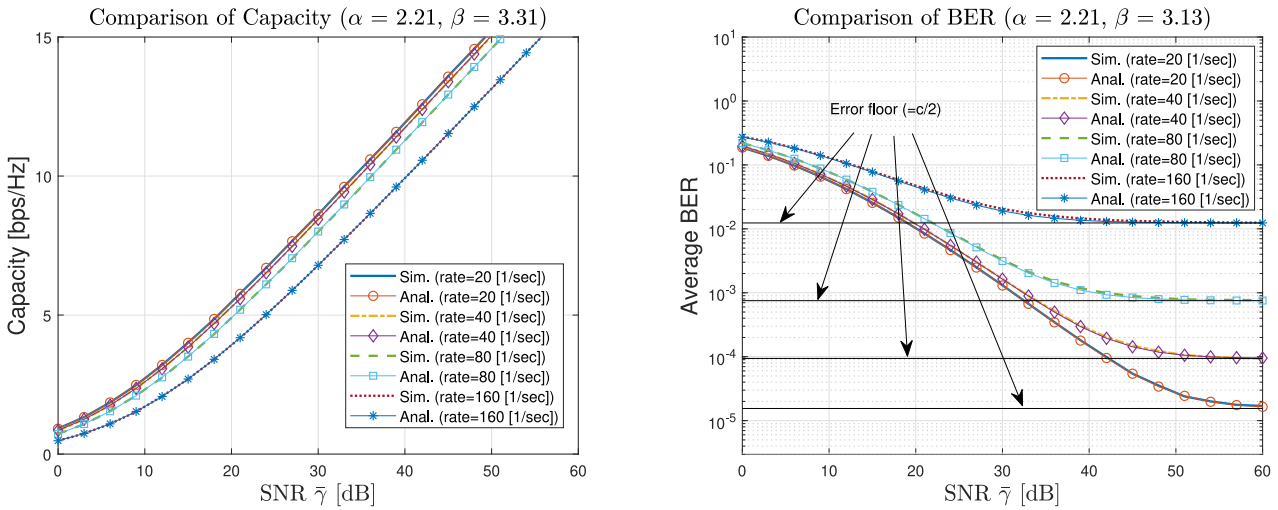

(a) Ergodic Capacity (b) Average BER

FIGURE 5. The results of the performance analysis with respect to different bubble generation rate under the given mean radius of $\mu_R = 1.50$ [mm] and horizontal movement of $\sigma_X = 5$ [mm] of a bubble.

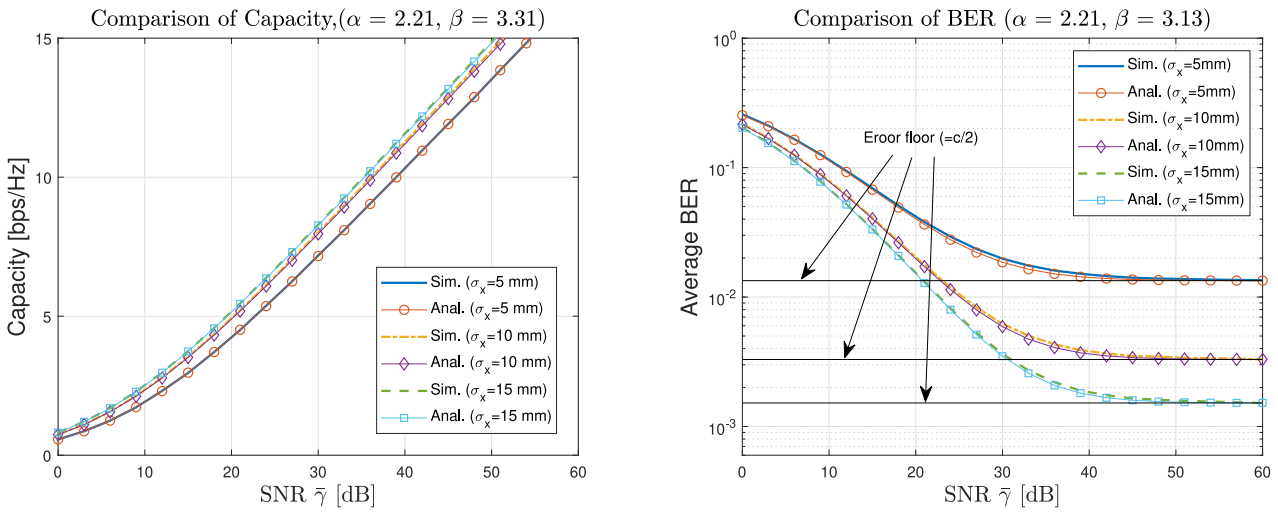

(a) Ergodic Capacity (b) Average BER

FIGURE 6. The results of the performance analysis with respect to different horizontal movement under the given mean radius of $\mu_R = 1.95$ [mm] and generation rate of 80 [1/sec] of a bubble.

using this PDF with those using the corresponding simulation data, which are shown in Figs. 4-6. Throughout the figures, we note that the analytic results derived with our proposed statistical model fit well with the simulation data.

Fig. 4 presents the results of performance analysis as a function of mean radius of air bubble. In both sub-figures, we see that the complete obstruction due to the air bubbles can significantly degrade both performance metrics. In Fig. 4(a), we observe that the perfect blockage with the probability value c will affect the slope of ergodic capacity with respect to SNR, also known as multiplexing gain or degree of freedom. With the results of average BER in 4(b), we see that each BER has an error floor with a value $\frac{c}{2}$ drawn in black color. In other words, we can see the average BER in (25)

$$P_b \approx \frac{c}{2} + \sum_{i=1}^{n} \frac{C_i^{(2)}}{4\pi} \left(\frac{p^2 q}{2}\right)^{-\frac{\alpha+\beta}{4}} G_{2,5}^{4,2}\left(\begin{matrix} 1-\frac{\alpha+\beta}{4}, \frac{1}{2}-\frac{\alpha+\beta}{4} \\ \frac{\alpha-\beta}{4}, \frac{\alpha-\beta+2}{4}, -\frac{\alpha-\beta}{4}, -\frac{\alpha-\beta-2}{4}, -\frac{\alpha+\beta}{4} \end{matrix} \middle| \frac{{z_i}^2}{8p^2 q} \right)$$
$$+ \frac{C_i^{(2)}}{4\pi} \left(\frac{p^2 q}{2}\right)^{-\frac{\alpha+\beta}{4}} G_{2,5}^{4,2}\left(\begin{matrix} 1-\frac{\alpha+\beta}{4}, \frac{1}{2}-\frac{\alpha+\beta}{4} \\ \frac{\alpha-\beta}{4}, \frac{\alpha-\beta+2}{4}, -\frac{\alpha-\beta}{4}, -\frac{\alpha-\beta-2}{4}, -\frac{\alpha+\beta}{4} \end{matrix} \middle| \frac{{z_0}^2}{8p^2 q} \right) \quad (25)$$

converges with $\frac{c}{2}$ as SNR tends to infinity. This implies that when the air bubbles exist in the path of the UWOC link, they cause a fade in SNR over time until they start to rise. In that case, the design the compensation techniques to mitigate the effect of deep fading by air bubbles is required, e.g., forward error correction (FEC), automatic repeat request (ARQ), interleaver, etc.

Fig. 5 illustrates the results of both performance metrics with respect to different bubble generation rates. As the bubble generation rate increases, the ergodic capacity and average BER become worse. This is because more bubbles might probably occur on beam propagation path due to the increased generation of air bubbles. On other front, we show in Fig. 6 the effect of system performance for different value of standard deviation for horizontal movement of air bubbles. We see that increased horizontal movement can help improving both performances. When the rising bubbles are more scattered due to the variation of water flow and pressure, the bubbles might be spread out over beam aperture in probability and thus the obstruction can be reduced.

V. CONCLUSION

In this paper, we developed a statistical model describing the received power obstructed by air bubbles in a UWOC channel. Our proposed model is based on three random variables: which are the horizontal movement, the size and the generation of a bubble. Based on the statistics of those random behavior of air bubbles, we derived the received power and its moments. By using the method of moments, we find suitable distribution fitting the simulation data. We derived the distribution of the received power as a combination of the well-known Weibull distribution and two of the Dirac delta functions. We verified goodness of fit for our proposed statistical model using the *MSE* and the R^2 tests. Finally, we combined our statistical model of air bubble obstruction with a Gamma-Gamma turbulence model and analyzed the performance over this composite channel model. We confirmed that the approximated analytic results were well matched with the simulation results.

APPENDIX
STATISTICAL MODEL USING METHOD OF MOMENTS

A. NOTATIONS

(1) The radius of bubble: R_i
(2) The radius of the receiver aperture: r
(3) The distance between the center of a bubble and the line that is perpendicular to the bottom of the tank and goes through the center of the beam: X_i
(4) The time duration until the current time instant of a bubble generated in the i time interval in the past: T_i
(5) The height of a bubble: $H_i = h_i(T_i, R_i) = v(R_i)T_i$
(6) The distance between the center of a bubble and that of the beam: $D_i = d_i(X_i, H_i) = \sqrt{X_i^2 + (H_i - 0.105)^2}$
(7) The distribution of the Gaussian beam: $h(w, z)$
(8) The power obstructed by each bubble: $B_i = b_i(X_i, R_i, T_i)$

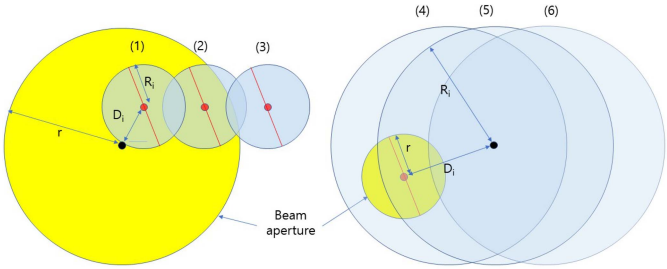

FIGURE 7. The six cases of bubbles overlapping the beam aperture.

B. CASES OF THE OBSTRUCTED POWER

We can divide the obstructed power into six cases depending on where the bubble's location and size with respect to the beam. Fig. 7 presents a pictorial description of each case. We will derive the six cases separately as follows.

(1) $r \geq R_i$, $D_i \leq r - R_i$: When the bubble is completely inside the beam area,

$$B_i^{(1)} = b_i^{(1)}(X_i, R_i, T_i) = \int_{-R_i}^{R_i} \int_{-\sqrt{R_i^2 - w^2} - D_i}^{\sqrt{R_i^2 - w^2} - D_i} h(w, z)\, dz\, dw. \quad \text{(A.1)}$$

(2) $r \geq R_i$, $D_i > r - R_i$, $D_i^2 \leq r^2 - R_i^2$: When the bubble partially overlaps with the beam aperture and one of the diameters passing through the center of bubble is entirely contained in the aperture,

$$B_i^{(2)} = b_i^{(2)}(X_i, R_i, T_i) = \int_{-R_i}^{R_i} \int_{-\sqrt{R_i^2 - w^2} - D_i}^{\sqrt{R_i^2 - w^2} - D_i} h(w, z)\, dz\, dw - \int_{-\sqrt{r^2 - \frac{R_i^2 - r^2 - D_i^2}{2D_i}}}^{\sqrt{r^2 - \frac{R_i^2 - r^2 - D_i^2}{2D_i}}} \int_{-\sqrt{R_i^2 - w^2} - D_i}^{-\sqrt{r^2 - w^2}} h(w, z)\, dz\, dw. \quad \text{(A.2)}$$

(3) $r \geq R_i$, $D_i^2 > r^2 - R_i^2$, $D_i \leq r + R_i$: When the bubble partially overlaps with the beam aperture and no diameter of the bubble is contained in the aperture,

$$B_i^{(3)} = b_i^{(3)}(X_i, R_i, T_i) = \int_{-\sqrt{r^2 - \frac{R_i^2 - r^2 - D_i^2}{2D_i}}}^{\sqrt{r^2 - \frac{R_i^2 - r^2 - D_i^2}{2D_i}}} \int_{-\sqrt{r^2 - w^2}}^{\sqrt{R_i^2 - w^2} - D_i} h(w, z)\, dz\, dw. \quad \text{(A.3)}$$

(4) $r < R_i$, $D_i \leq R_i - r$: When the beam aperture is completely inside the bubble area,

$$B_i^{(4)} = b_i^{(4)}(X_i, R_i, T_i) = \int_{-r}^{r} \int_{-\sqrt{r^2 - w^2}}^{\sqrt{r^2 - w^2}} h(w, z)\, dz\, dw \triangleq m. \quad \text{(A.4)}$$

(5) $r < R_i$, $D_i > R_i - r$, $D_i^2 \leq R_i^2 - r^2$: When the bubble partially overlaps with the beam aperture and one of the

diameters of the beam aperture is entirely contained in the bubble,

$$B_i^{(5)} = b_i^{(5)}(X_i, R_i, T_i) = \int_{-r}^{r} \int_{-\sqrt{r^2-w^2}}^{\sqrt{r^2-w^2}} h(w,z)\,dz\,dw - \int_{\sqrt{r^2-\frac{R_i^2-r^2-D_i^2}{2D_i}}}^{-\sqrt{r^2-\frac{R_i^2-r^2-D_i^2}{2D_i}}} \int_{\sqrt{R_i^2-w^2}-D_i}^{\sqrt{r^2-w^2}} h(w,z)\,dz\,dw. \tag{A.5}$$

(6) $r < R_i$, $D_i^2 > R_i^2 - r^2$, $D_i \le r + R_i$: when the bubble overlaps with the beam aperture and no diameter of the beam aperture is contained in the bubble,

$$B_i^{(6)} = b_i^{(6)}(X_i, R_i, T_i) = \int_{-\sqrt{r^2-\frac{R_i^2-r^2-D_i^2}{2D_i}}}^{\sqrt{r^2-\frac{R_i^2-r^2-D_i^2}{2D_i}}} \int_{-\sqrt{r^2-w^2}}^{\sqrt{r^2-w^2}-D_i} h(w,z)\,dz\,dw. \tag{A.6}$$

C. CALCULATIONS OF MOMENTS FOR TOTALLY OBSTRUCTED POWER B

(1) *The first moment of B:* The expectation of the ith bubble is given on the bottom of the page by (A.7). We note that $f_{X_i}(x)$, $f_{R_i}(r)$, and $f_{T_i}(t)$ are the distributions of horizontal movement X_i, radius R_i, and generation time T_i, of air bubble, respectively, which are given in Section II. The expectation of the sum of the obstructed power by the $10/L$ bubbles, which are all the generated bubbles during the overall time duration of 10 [sec] at a generation rate $1/L$, is given by

$$\mathbb{E}[B] = \sum_{i=1}^{10/L} \mathbb{E}[B_i]. \tag{A.8}$$

(2) *The second moment of B:* The second moment the ith bubble is given on the bottom of the page by (A.9). The second moment of the sum of the obstructed power is represented as

$$\mathbb{E}\left[B^2\right] = \sum_{i=1}^{10/L} \mathbb{E}\left[B_i{}^2\right] + 2\sum_{i=1}^{10/L}\sum_{j=1}^{10/L} \mathbb{E}[B_i]\mathbb{E}[B_j]. \tag{A.10}$$

D. PARAMETER ESTIMATION

To begin, we assume the distribution of the power obstructed by air bubbles follows the form of $a\delta(x) + bf(x)$ $(x \ge 0)$, where $f(x)$ can be determined by any suitable density function. Here, a is the probability of no power obstruction, i.e., no bubble obstructs the power. The probability of each bubble not obstructing the power can be calculated as

$$\int_{(i-1)L}^{iL} \int_{0}^{0.01} \int_{-\infty}^{\infty} \mathbb{1}_{(r+R_i,\infty)}(D_i)\,dx f_{R_i}(r_i)\,dr_i f_{T_i}(t) dt_i \tag{A.11}$$

Therefore, a is given on the bottom of the page by (A.12). We note that $b = 1 - a$, because $\int_0^\infty a\delta(x) + bf(x)\,dx = 1$.

Based on the observation of right tail distribution from simulation data, we now model $f(x)$ as the Weibull distribution, which is represented as

$$f(x) = f_W(x) = \begin{cases} \frac{k}{\lambda}\left(\frac{x}{\lambda}\right)^{k-1} e^{(x/\lambda)^k}, & x \ge 0, \\ 0, & x < 0. \end{cases} \tag{A.13}$$

Here, we have two parameters k and λ to estimate. The expectation and the second moment of the distribution $a\delta(x) + bf_W(x)$ are $b\lambda\Gamma(1+\frac{1}{k})$ and $b\lambda^2\Gamma(1+\frac{2}{k})$, respectively. Letting $\mathbb{E}[B] = b\lambda\Gamma(1+\frac{1}{k})$ and $\mathbb{E}[B^2] = b\lambda^2\Gamma(1+\frac{2}{k})$, we obtain k by solving the following equation.

$$\mathbb{E}^2[B]\Gamma\left(1+\frac{2}{k}\right) = b\mathbb{E}\left[B^2\right]\Gamma^2\left(1+\frac{1}{k}\right). \tag{A.14}$$

Then, λ can be obtained by solving one of two moments with the obtained k.

REFERENCES

[1] H. Kaushal and G. Kaddoum, "Underwater optical wireless communication," *IEEE Access*, vol. 4, pp. 1518–1547, 2016.
[2] C. Shen *et al.*, "20-meter underwater wireless optical communication link with 1.5 Gbps data rate," *Opt. Exp.*, vol. 24, no. 22, pp. 25502–25509, Oct. 2016.

$$\mathbb{E}[B_i] = \int_{(i-1)L}^{iL} \left[\int_0^{0.01} \left[\int_{-\infty}^{\infty} b_i(x_i, r_i, t_i) f_{X_i}(x_i)\,dx_i \right] f_{R_i}(r_i)\,dr_i \right] f_{T_i}(t_i)\,dt_i \tag{A.7}$$

$$\mathbb{E}\left[B_i{}^2\right] = \int_{(i-1)L}^{iL} \left[\int_0^{0.01} \left[\int_{-\infty}^{\infty} b_i{}^2(x_i, r_i, t_i) f_{X_i}(x_i)\,dx_i \right] f_{R_i}(r_i)\,dr_i \right] f_{T_i}(t_i)\,dt_i \tag{A.9}$$

$$a = \prod_{i=1}^{10/L} \int_{(i-1)L}^{iL} \left[\int_0^{0.01} \left[\int_{-\infty}^{\infty} \mathbb{1}_{(r+R_i,\infty)}(D_i)\,dx \right] f_{R_i}(r_i)\,dr_i \right] f_{T_i}(t_i)\,dt_i \tag{A.12}$$

[3] C. Li, K.-H. Park, and M.-S. Alouini, "On the use of a direct radiative transfer equation solver for path loss calculation in underwater optical wireless channels," *IEEE Wireless Commun. Lett.*, vol. 4, no. 5, pp. 561–564, Oct. 2015.
[4] H. Gao and H. Zhao, "A fast-forward solver of radiative transfer equation," *Transp. Theory Stat. Phys.*, vol. 38, no. 3, pp. 149–192, 2009.
[5] E. Illi, F. E. Bouanani, K.-H. Park, F. Ayoub, and M.-S. Alouini, "An improved accurate solver for the time-dependent RTE in underwater optical wireless communications," *IEEE Access*, vol. 7, pp. 96478–96494, 2019.
[6] R. Leathers, T. Downes, C. O. Davis, and C. Mobley, *Monte Carlo Radiative Transfer Simulations for Ocean Optics: A Practical Guide*. Washington, DC, USA: Naval Res. Lab., Sep. 2004, p. 54.
[7] Z. Zeng, S. Fu, H. Zhang, Y. Dong, and J. Cheng, "A survey of underwater optical wireless communications," *IEEE Commun. Surveys Tuts.*, vol. 19, no. 1, pp. 204–238, 1st Quart., 2017.
[8] J. B. Graham Perspectives on Ocean Science Lecture Series. (2018). *There's More to Ocean Bubbles Than You Might Think*. [Online]. Available: https://www.uctv.tv/shows/Theres-More-to-Ocean-Bubbles-Than-You-Might-Think-33487
[9] E. Zedini, H. M. Oubei, A. Kammoun, M. Hamdi, B. S. Ooi, and M.-S. Alouini, "Unified statistical channel model for turbulence-induced fading in underwater wireless optical communication systems," *IEEE Trans. Commun.*, vol. 67, no. 4, pp. 2893–2907, Apr. 2019.
[10] M. V. Jamali *et al.*, "Statistical studies of fading in underwater wireless optical channels in the presence of air bubble, temperature, and salinity random variations," *IEEE Trans. Commun.*, vol. 66, no. 10, pp. 4706–4723, Oct. 2018.
[11] H. M. Oubei, R. T. ElAfandy, K.-H. Park, T. K. Ng, M.-S. Alouini, and B. S. Ooi, "Performance evaluation of underwater wireless optical communications links in the presence of different air bubble populations," *IEEE Photon. J.*, vol. 9, no. 2, pp. 1–9, Apr. 2017.
[12] S. H. Park, C. Park, J. Lee, and B. Lee, "A simple parameterization for the rising velocity of bubbles in a liquid pool," *Nucl. Eng. Technol.*, vol. 49, no. 4, pp. 692–699, Oct. 2017.
[13] K. O. Bowman and L. R. Shenton, "Method of moments," *Encyclopedia of Statistical Sciences*, vol. 5. New York, NY, USA: Wiley, 1985, pp. 2092–2098.
[14] A. A. Farid and S. Hranilovic, "Outage capacity optimization for free-space optical links with pointing errors," *J. Lightw. Technol.*, vol. 25, no. 7, pp. 1702–1710, Jul. 2007.
[15] I. S. Ansari, F. Yilmaz, and M.-S. Alouini, "Performance analysis of free-space optical links over Málaga ($\mathcal{M}$) turbulence channels with pointing errors," *IEEE Trans. Wireless Commun.*, vol. 15, no. 1, pp. 91–102, Jan. 2016.
[16] V. S. Adamchik and O. I. Marichev, "The algorithm for calculating integrals of hypergeometric type functions and its realization in REDUCE system," in *Proc. Int. Symp. Symb. Algebraic Comput. (ISSAC' 90)*, 1990, pp. 212–224.
[17] H. G. Sandalidis, T. A. Tsiftsis, G. K. Karagiannidis, and M. Uysal, "BER performance of FSO links over strong atmospheric turbulence channels with pointing errors," *IEEE Commun. Lett.*, vol. 12, no. 1, pp. 44–46, Jan. 2008.
[18] M. Elamassie and M. Uysal, "Vertical underwater VLC links over cascaded Gamma-Gamma turbulence channels with pointing errors," in *Proc. IEEE Int. Black Sea Conf. Commun. Netw. (IEEE BlackSeaCom 2019)*, Sochi, Russia, Jun. 2019, pp. 1–5.
[19] L. C. Andrews and R. L. Phillips, *Laser Beam Propagation Through Random Media*, 2nd ed. Bellingham, WA, USA: SPIE, 2005.
[20] M. Cheng, L. Guo, and Y. Zhang, "Scintillation and aperture averaging for Gaussian beams through non-Kolmogorov maritime atmospheric turbulence channels," *Opt. Exp.*, vol. 23, no. 25, pp. 32606–32621, Dec. 2015.

MYOUNGKEUN SHIN was born in Seoul, South Korea. He received the bachelor's degree in mathematical sciences from Seoul National University, Seoul, in 2011, and the master's degree in applied mathematics and computational science from the King Abdullah University of Science and Technology, Thuwal, Saudi Arabia, in 2019. He is currently pursuing the Ph.D. degree. His current research interests lie in partial differential equations and hydrodynamic limits and kinetic theory for dilute polymeric systems.

KI-HONG PARK (Senior Member, IEEE) was born in Suwon, South Korea. He received the B.Sc. degree in electrical, electronic, and radio engineering from Korea University, Seoul, South Korea, in 2005, and the joint M.S. and Ph.D. degrees from the School of Electrical Engineering, Korea University, in 2011. He joined the King Abdullah University of Science and Technology, Thuwal, Saudi Arabia, in 2011, as a Postdoctoral Fellow, where he has been a Research Scientist of electrical engineering with the Division of Computer, Electrical, Mathematical Science and Engineering since 2014. His research interests include communication theory and its application to the design and performance evaluation of wireless communication systems and networks. His research interests include the application to underwater visible light communication, optical wireless communications, unmanned aerial vehicle communication, and physical layer secrecy.

MOHAMED-SLIM ALOUINI (Fellow, IEEE) was born in Tunis, Tunisia. He received the Ph.D. degree in electrical engineering from the California Institute of Technology, Pasadena, CA, USA, in 1998. He joined the King Abdullah University of Science and Technology, Thuwal, Saudi Arabia, as a Professor of electrical engineering in 2009. He served as a Faculty Member with the University of Minnesota, Minneapolis, MN, USA, then with the Texas A&M University at Qatar, Education City, Doha, Qatar. His current research interests include the modeling, design, and performance analysis of wireless communication systems.